

# Water Vapour Exchange between Atmospheric Boundary Layer and Free Troposphere over Eastern China: Seasonal Characteristics and ENSO Anomaly

Xipeng Jin<sup>1</sup>, Xuhui Cai<sup>2\*</sup>, Xuesong Wang<sup>2</sup>, Qianqian Huang<sup>3</sup>, Yu Song<sup>2</sup>, Ling Kang<sup>2</sup>, Hongsheng Zhang<sup>4</sup>, Tong Zhu<sup>2</sup>

<sup>1</sup>Collaborative Innovation Center of Atmospheric Environment and Equipment Technology, Jiangsu Key Laboratory of Atmospheric Environment Monitoring and Pollution Control, School of Environmental Science and Engineering, Nanjing University of Information Science & Technology, Nanjing 210044, China

<sup>2</sup>State Key Lab of Environmental Simulation and Pollution Control, College of Environmental Sciences and Engineering, Peking University, Beijing 100871, China

<sup>3</sup>Institute of Urban Meteorology, Beijing 100089, China

<sup>4</sup>Department of Atmospheric and Oceanic Sciences, School of Physics, Peking University, Beijing 100871, China

*Correspondence to:* Xuhui Cai (E-mail: xhcai@pku.edu.cn)

1 **Abstract.** This study develops a quantitative climatology of water vapour exchange between  
2 the atmospheric boundary layer (ABL) and free troposphere (FT) over eastern China. The  
3 exchange flux is estimated for January, April, July, and October over 7 years based on a water  
4 vapour budget equation using simulated meteorological data. The spatiotemporal  
5 characteristics and occurrence mechanism of ABL-FT water vapour exchange and its  
6 relationship with ENSO are revealed: (1) The vertical exchange flux varies regionally and  
7 seasonally, with downward transport to maintain ABL moisture during winter and autumn in  
8 the northern region and persistent output to humidify FT in the southern region, particularly in  
9 summer. Additionally, the vertical exchange flux is also topographic dependent. (2) The  
10 vertical motion at the ABL top, which is produced by the dynamic forcing of the terrain on  
11 synoptic winds, is the dominant mechanism for the water vapour vertical exchange over the  
12 long-term average. The evolution of the vertical exchange flux within one-day scale is driven  
13 by the ABL diurnal cycle. (3) The interannual variation of water vapour vertical exchange is  
14 correlated with ENSO. A triple antiphase distribution with negative-positive-negative  
15 anomalies from north to south exists in La Niña years (and vice versa in El Niño years), which  
16 corresponds to the spatial pattern of anomalous precipitation. This phenomenon is mainly due  
17 to the alteration of vertical velocity and water vapour content at the ABL top varying with  
18 ENSO phases. These results provide new insight into understanding the atmospheric water  
19 cycle.

20 **Keywords:** Water vapour; atmospheric boundary layer; free troposphere; vertical exchange

## 21 **1 Introduction**

22 Water vapour is a significant constituent in the atmosphere. It directly participates in  
23 fundamental physical processes, including cloud formation, precipitation, severe weather  
24 development and atmospheric circulation (Sodemann and Stohl, 2013; Wong et al., 2018;  
25 Wypych et al., 2018). Water vapour also affects important chemical reactions, such as  
26 providing OH radicals for gaseous photochemical transformations and serving as a medium in  
27 secondary aerosol formations (Pilinis et al., 1989; Tabazadeh 2000; Wu et al., 2019). Moreover,  
28 the radiation forcing of water vapour accounts for about 2/3 of the total natural greenhouse  
29 effect, which plays a vital role in climate feedback (Kiehl and Trenberth, 1997; Harries et al.,  
30 2008; Adebisi et al., 2015).

31 The distribution of water vapour in the atmospheric system depends on its source and  
32 transport processes. In general, water vapour evaporates from the Earth's surface into the  
33 atmosphere. From the meridional and zonal view, it presents a transport trend from low latitude  
34 to high latitude and from ocean to land. The horizontal transport of water vapour has been  
35 widely discussed from multiple scales. Hemispheric-scale atmospheric rivers induce large  
36 excursions of high vertically integrated water vapour from the subtropics to high latitudes  
37 (Newell et al. 1992; Zhu and Newell 1998; Sodemann and Stohl, 2013). Synoptic-scale  
38 moisture flux convergence of extratropical cyclones explains the precipitations and cloud  
39 structures over the warm front and cold front (Boutle et al., 2010; Wong et al., 2018). Regional-  
40 scale transport processes are widely reported in many areas from water vapour advection and  
41 dynamical convergence (Zhou and Yu, 2005; Sun et al., 2010; Gvozdikova and Muller, 2021).  
42 However, these studies estimate vertically integrated water vapour through the atmospheric  
43 layer (usually from the surface to 300 hPa) or only focused on a certain altitude.

44 The water vapour vertical transport, especially within the troposphere, plays a key role in  
45 the atmospheric water cycle. All water vapour in the atmosphere originates from surface  
46 evaporation and is first confined in the atmospheric boundary layer (ABL, Boutle et al., 2010),  
47 which is defined as the lowest layer of the atmosphere influenced by the Earth's surface (Stull,  
48 1988). The water vapour is turbulently mixed in the ABL, making it act as a reservoir. Actually,  
49 all water vapour entering and transporting meridionally and zonally in the free troposphere  
50 (FT) is initially exported through the ABL (Bailey et al., 2013). In other words, the water  
51 vapour exchange between the ABL and the FT is a prerequisite for its large-scale transport and  
52 redistribution, as well as interaction with other constituents, in the upper atmosphere. Several  
53 studies indicate the importance of this key process on precipitation (Liu et al., 2020), cloud  
54 systems (Miura et al., 2007), tropical cyclone formation (Fritz and Wang, 2013), Madden–  
55 Julian oscillation (Hirota et al., 2018), West African Monsoon Jump (Hagos and Cook, 2007),  
56 and O<sub>3</sub> vertical distributions (Andrey et al., 2014). Therefore, it is of great significance to  
57 quantify the vertical exchange of water vapour between the ABL and FT.

58 However, the exchange between the ABL and FT is not straightforward, both for water  
59 vapour and air mass. Although the diurnal variation of the ABL depth allows air constituents

60 to be entrained into and left out of this layer within its variation range, the actual exchange  
61 between ABL and FT is small on the time scale of more than one day due to the cancelling  
62 effect (Hov and Flatoy, 1997; Jin et al., 2021). The current studies on water vapour vertical  
63 transport are mainly limited to complex terrain areas or special convective events. The  
64 local/mesoscale circulation induced by orographic thermal and dynamic effects is considered  
65 a key process for ABL ventilation (Kossmann et al., 1999; McKendry and Lundgren, 2000;  
66 Dacre et al., 2007). Henne et al. (2005) found that there were elevated moisture layers in the  
67 lower free troposphere in the lee of the Alps resulting from mountain venting. On average for  
68 the 12-year period, ~30% of the water vapour of the Alpine boundary layer was vented to the  
69 FT per hour during the daytime, which makes the total precipitable water within the elevated  
70 moisture layer increase by ~1.3 mm. Another simulated study indicates that the moisture  
71 exchange between the ABL and FT of mountainous topography can be about 3–4 times larger  
72 than the amount of moisture evaporated from the surface in a specific ventilation event (Weigel  
73 et al., 2007). The convective system, mainly mesoscale deep and shallow convection, is another  
74 important factor leading to the vertical transport of water vapour. The isotope observations  
75 show that the moisture transport pathways to the subtropical North Atlantic FT are linked to  
76 dry convection processes over the African continent which effectively injects humidity from  
77 the ABL to higher altitudes (Gonzalez et al., 2016; Dahinden et al., 2021). The water vapour  
78 budget of the free troposphere of the maritime tropics shows that 20% of this source comes  
79 from vertical convective transport (Sherwood, 1996). On the other hand, an idealized  
80 simulation suggests that the warm conveyor belt ascent and shallow convective processes  
81 contributed about equally to FT moisture (Boutle et al., 2010, 2011).

82 Though for these studies, general characteristics of long-term and wide-ranging ABL-FT  
83 water vapour exchange are still unknown. These characteristics are closely bound up with the  
84 atmospheric energy flow and the entire climate system, affecting clouds, precipitation and  
85 radiation (Sodemann and Stohl, 2013; Wong et al., 2018; Wypych et al., 2018). For example,  
86 small variations in upper atmospheric humidity over a large space-time scale can cause  
87 systemic changes in the hydrological cycle and atmospheric circulation (Minschwaner and  
88 Dessler, 2004; Sherwood et al., 2010; Allan, 2012). The climate state of water vapour vertical  
89 exchange flux is critical for quantifying these specific effects. To fill this knowledge gap, the  
90 present study calculates the water vapour exchange flux between the ABL and FT for 7 years  
91 (2011&2014-2019) over eastern China (20-42°N, 108-122°E) to establish the first quantitative  
92 climatology view on this issue. The water vapour budget method is used, with the mesoscale  
93 meteorological simulation providing input data. January, April, July, and October, respectively  
94 representing winter, spring, summer, and autumn, are considered to discuss the seasonal  
95 characteristics. Interannual differences are analysed by investigating the impact of El Niño and  
96 La Niña events. On the basis of understanding the foundational features, we further attempt to  
97 discuss the role of ABL-FT water vapour exchange playing in anomalous precipitation. The  
98 arrangement of this paper is as follows. Data and methods are described in Section 2. The  
99 seasonal characteristics and mechanism analysis, interannual variability and the relation with

100 anomalous precipitation are presented and discussed in Section 3. Finally, the findings of this  
101 study are summarized in Section 4.

## 102 **2 Data and methods**

### 103 **2.1 Observation data**

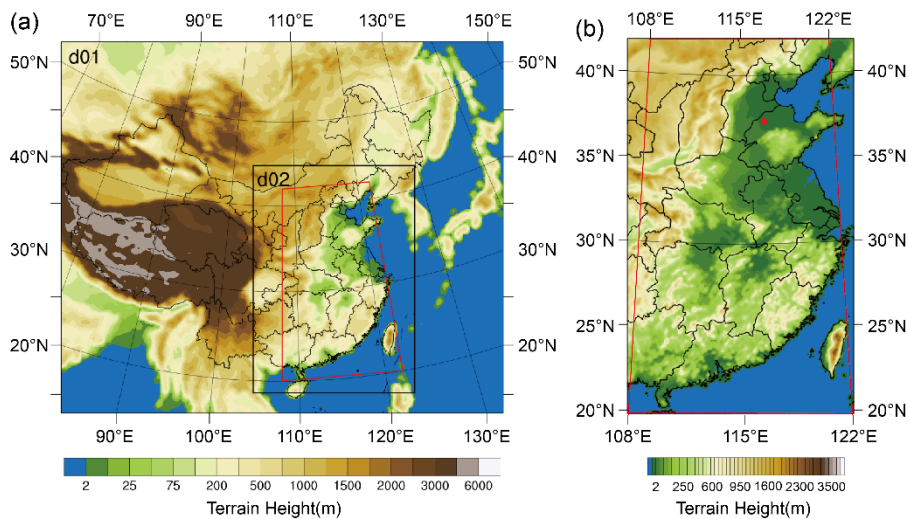
104 Intensive ABL sounding data and routine surface meteorological data were used to  
105 evaluate the performance of the Weather Research Forecast (WRF) model that provided the  
106 input data for estimating exchange flux.

107 Intensive ABL sounding data: Two field experiments of intensive GPS (Global  
108 Positioning System) sounding were carried out in Dezhou (37°16' N, 116°43' E), located in the  
109 middle of the North China Plain (NCP) (Fig. 1b), from December 25, 2017, to January 24,  
110 2018, and from May 14 to June 14, 2018. Eight soundings were taken for each day, at 02:00,  
111 05:00, 08:00, 11:00, 14:00, 17:00, 20:00 and 23:00 LT (i.e., UTC + 8). GPS radiosonde  
112 (Beijing Changzhi Sci and Tech Co. Ltd., China) was used to obtain profiles of wind,  
113 temperature and humidity with the ascending velocity being about 3-5 m s<sup>-1</sup>. We eliminated  
114 the outliers from the original data and averaged the profiles to an effective vertical resolution  
115 of 10 m. ABL heights were determined with these data via the potential temperature profile  
116 method (Liu and Liang, 2010). The reliability of the GPS sounding data has been systematically  
117 evaluated by Li et al. (2020) and Jin et al. (2020).

118 Routine surface meteorological data: The hourly surface data of 137 routine observatories  
119 distributed within the research domain were collected from the Chinese National  
120 Meteorological Center. The dataset included information on wind speed and direction, air  
121 temperature, relative humidity, air pressure, cloud coverage and precipitation, which was used  
122 to evaluate the WRF simulation.

### 123 **2.2 Three-dimensional meteorological simulation**

124 The WRF model was conducted to provide three-dimensional meteorological data for the  
125 estimation of ABL-FT water vapour exchange flux. Two nested domains (Fig. 1a) were  
126 employed with horizontal grid lengths of 30 and 10 km, respectively. The inner covered eastern  
127 China (20–42°N, 108–122°E), the main research region for the ABL-FT water vapour  
128 exchange in the present work (Fig. 1b). Each domain had 37 vertical layers extending from the  
129 surface to 100 hPa, with the vertical resolution being about 20-30 m below 200 m, increasing  
130 to ~100 m at 750 m, ~250 m at 2000 m, ~350 m at 3000 m, ~600 m at 5000 m, ~900 m at 8000  
131 m, ~1300 m at 11000 m and gradually enlarging to the top of the model. There were 24 layers  
132 within 3 km to resolve the ABL and its upper FT. The meteorological initial and boundary  
133 conditions were set using the US National Center for Environmental Prediction Final Analysis  
134 (NCEP-FNL) dataset.



135

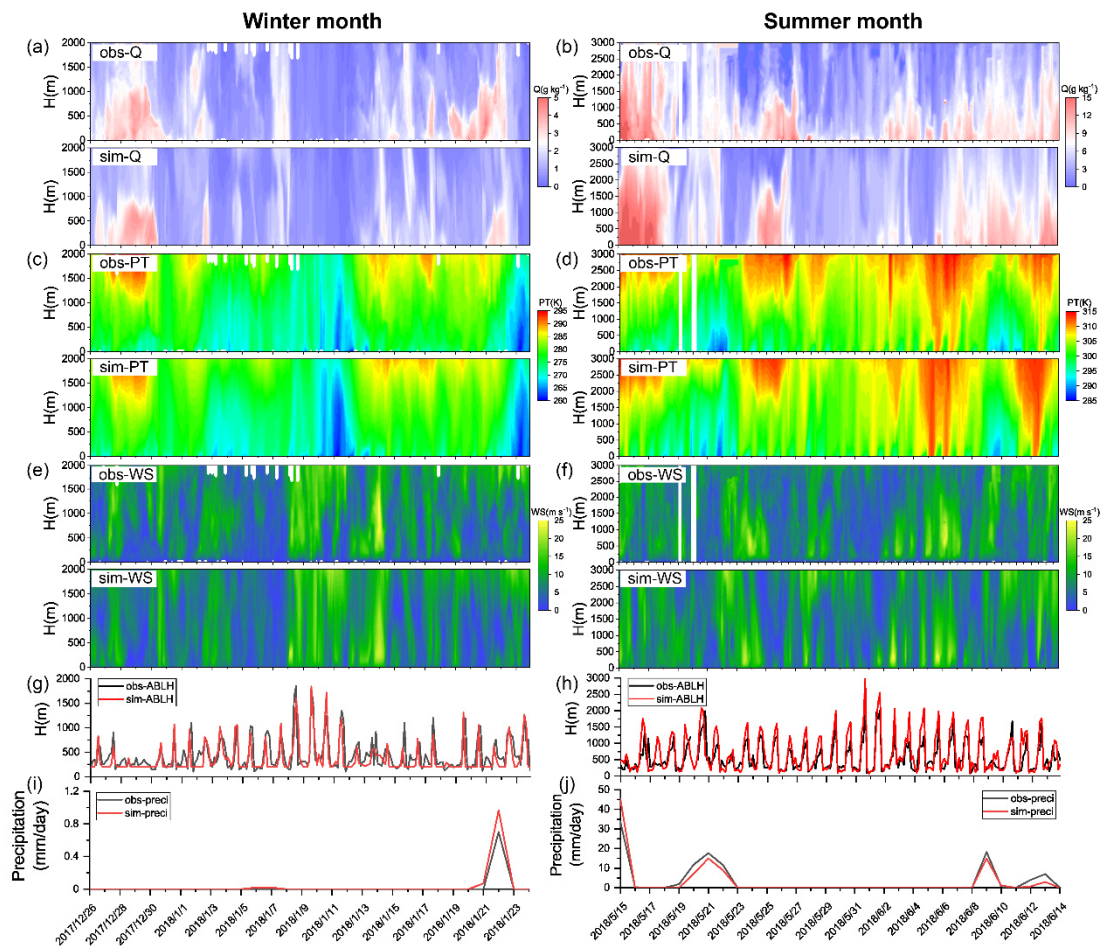
136 Figure 1. Geographical map of (a) the Weather Research and Forecast (WRF) model domains (d01 and  
 137 d02) and (b) the amplified research domain (marked with red lines). The map uses the Lambert  
 138 projection with the centre meridians of 108°E in (a) and 115°E in (b). The red dot in (b) indicates the  
 139 intensive GPS sounding observatory.

140 In order to adequately reproduce water vapour distribution and to correctly estimate the  
 141 ABL-FT exchange flux, sensitivity simulations were carried out to choose reasonable physical  
 142 parameterization schemes. We focused on the microphysical and cumulus parameterizations  
 143 that are the most relevant to the moisture simulation. Microphysics in the model includes  
 144 explicitly resolved water vapour, cloud and precipitation processes. Cumulus schemes are  
 145 responsible for the sub-grid scale effects of convection and/or shallow clouds. Vertical fluxes  
 146 due to unresolved updrafts and downdrafts are represented. Lin et al. scheme (Lin et al., 1983)  
 147 and WRF Single-Moment 6-class (WSM6) scheme (Hong and Lim, 2006) in microphysics  
 148 parameterization, and Grell-Devenyi (GD) ensemble scheme (Grell and Devenyi, 2002) and  
 149 Kain-Fritsch (KF) scheme (Kain, 2004) in cumulus parameterization were compared, which  
 150 were most commonly used in previous moisture simulation studies (Perez et al., 2010;  
 151 Gonzalez et al., 2013; Jain and Kar, 2017; Qian et al., 2020). Other physics parameterization  
 152 schemes used in this study included the Yonsei University PBL scheme (Hong et al., 2006),  
 153 the Noah land surface Model (Chen and Dudhia, 2001), the Dudhia shortwave radiation scheme  
 154 (Dudhia, 1989), and the rapid radiative transfer model (Mlawer et al., 1997) for longwave  
 155 radiation. WRF simulations were initialized at 00 UTC on the day and there was a 12-h spin-  
 156 up time before the start of each 48-h simulation. Domain outputs were sampled every hour for  
 157 the whole simulation period (January, April, July, and October in 2011 and 2014-2019).

158 These schemes were evaluated by comparing simulated and observed specific humidity,  
 159 temperature and wind speed, from their near-surface temporal evolution and vertical spatial  
 160 structure. Another two key parameters, ABL height and precipitation were also concerned: the  
 161 former directly affects the exchange flux results, and the latter characterizes the moisture  
 162 budget. The hourly averages of model outputs were extracted from the grid points nearest to  
 163 the observed sites for comparison. In the vertical direction, the modelled and sounding data

164 were simultaneously interpolated into the same height with 10 m intervals ranging from 50 m  
 165 to 3 km. Note that the ABL height was diagnosed with the potential temperature profile method  
 166 both for the simulations and for observation data, rather than using the default bulk Richardson  
 167 number method in the YSU scheme.

168 The results of sensitivity experiments showed that there were no appreciable differences  
 169 among various microphysical and cumulus parameterization schemes (Table S1 and S2). In  
 170 comparison, the combination of the WSM6 scheme and GD scheme performed better in  
 171 humidity simulation and was more effective in reproducing temperature, wind speed and ABL  
 172 height, especially in summer (Table S2). Therefore, these schemes were used in the present  
 173 study. Its simulation performance determines the reliability of the calculated flux results and  
 174 thus a comprehensive evaluation is provided here. The spatial-temporal evolutions of modelled  
 175 and observed meteorological fields are presented by the height-time cross sections of specific



176  
 177 Figure 2. Observed and simulated time-height cross-sections of (a-b) specific humidity, (c-d) potential  
 178 temperature, (e-f) wind speed, and temporal evolution of (g-h) ABL height and (i-j) daily cumulative  
 179 precipitation at the Dezhou site (37.27°N, 116.72°E) during winter (from December 26, 2017, to  
 180 January 24, 2018) and summer (from May 15, 2018, to June 14, 2018) months of intensive GPS  
 181 sounding field experiment. The time resolution of sounding data in (a-h) is 3-hr. The Y-axis scales are  
 182 different in the winter panel and the summer panel.

183 humidity, potential temperature and wind speed, as well as the ABL height and precipitation  
184 (Fig. 2). During the winter and summer months of the intensive GPS sounding, the simulated  
185 atmospheric thermal and dynamic structures were comparable with observations. The  
186 alternating between dry and wet atmospheric states (Fig. 2a-b), formation and decay of upper  
187 temperature inversion (Fig. 2c-d), and vertical location and temporal transition of the strong  
188 and weak wind layers (Fig. 2e-f) were successfully reproduced. Accordingly, a good  
189 correlation between the simulated and observed ABL height was achieved, both in terms of  
190 diurnal variation and synoptic evolution lasting several days (Fig. 2g-h). The correlation  
191 coefficients were 0.71 and 0.84 during wintertime and summertime, respectively. It should be  
192 mentioned that there was a slight discrepancy in the modelled ABL heights (mean biases are  
193 about -70 m and 120 m in winter and summer), which may further affect the identification of  
194 other parameters (such as the wind component) at the ABL top and lead to uncertainty in the  
195 calculation results. This impact will be quantitatively analysed in the discussion section.  
196 Another concerned meteorological factor, the daily cumulative precipitation was also  
197 evaluated, which showed a consistent evolution in observation and simulation (Fig. 2i-j) with  
198 correlation coefficients as high as 0.99 and 0.91 ( $p < 0.05$ ) in winter and summer respectively,  
199 demonstrating that the moisture budget is accurately captured by the WRF simulations.  
200 Overall, the model showed the ability to capture the major variation of observed atmospheric  
201 thermal-dynamical structures reasonably, which ensures the validity of the meteorological  
202 inputs for the ABL-FT exchange flux calculation.

### 203 2.3 ABL-FT water vapour exchange flux

204 Similar to mass vertical exchange (Sinclair et al. 2010; Jin et al., 2021), the estimation of  
205 ABL-FT water vapour exchange flux in this study was based on an ABL water vapour budget  
206 equation established by Boutle et al. (2010):

$$\begin{aligned}
207 \quad \frac{\partial}{\partial t} \left( \int_0^h \rho q dz \right) = & - \left( \frac{\partial}{\partial x} \int_0^h \rho q u dz + \frac{\partial}{\partial y} \int_0^h \rho q v dz \right) + (\rho q)_h \left( \frac{\partial h}{\partial t} \right) \\
208 \quad & - (\rho q)_h (\vec{U} \cdot \vec{n})_h - (\overline{\rho w' q'})_h + (\overline{\rho w' q'})_0 + P, \quad (1)
\end{aligned}$$

209 where  $\rho$  is air density,  $q$  is water vapour mixing ratio,  $h$  is the ABL height,  $\vec{U} = (u, v, w)$  is  
210 wind vector,  $\vec{n} = (-\frac{\partial h}{\partial x}, -\frac{\partial h}{\partial y}, 1)$  is the unit normal vector perpendicular to the ABL top  
211 surface,  $w'$  and  $q'$  are the fluctuation values of vertical velocity and water vapour content  
212 respectively.  $P$  is the precipitation. Subscripts  $h$  and  $0$  indicate quantities at the ABL top and  
213 the surface. The first term on the right side of Eq. (1) represents horizontal  
214 convergence/divergence within the ABL, the second term indicates the local change in ABL  
215 depth, the third term indicates vertical advection across the ABL top, the fourth and fifth terms  
216 are turbulent transport at the ABL top and the surface respectively, and the last term indicates  
217 the net precipitation falling through the ABL.

218 Denoting the water vapour vertical exchange flux between the ABL and FT as  $F$  (positive  
219 values represent upward transport), it can be further written as:

$$\begin{aligned}
220 \quad F &= -((\rho q)_h \left( \frac{\partial h}{\partial t} \right) - (\rho q)_h (\vec{U} \cdot \vec{n})_h - (\overline{\rho w'q'})_h) \\
221 \quad &\approx -((\rho q)_h \frac{\partial h}{\partial t} + (\rho q)_h \left( u_h \frac{\partial h}{\partial x} + v_h \frac{\partial h}{\partial y} \right) - (\rho q)_h w_h). \quad (2)
\end{aligned}$$

222 Since turbulent transport between the ABL and FT is typically related with dryer air that does  
223 not affect the total moisture content,  $(\overline{w'q'})_h$  is usually considered to be a negligible  
224 contribution to the ABL-FT water vapour exchange flux (Boutle et al., 2010). Specifically, the  
225 finite difference method was adopted for calculation with the time step being 1 hr, and the  
226 horizontal dimensions of the model grid being 10 km. The ABL heights were obtained from  
227 the hourly output of the WRF model. Other variables were extracted from the vertical level  
228 closest to the top of the ABL. It is clear that the water vapour vertical exchange flux between  
229 the ABL and FT is determined by i) the local temporal variation of ABL height,  $\frac{\partial h}{\partial t}$ , allowing  
230 the water vapour entrained into the ABL or left in the upper atmosphere; ii) the spatial variation  
231 of the ABL, making water vapour horizontally advected across an inclined ABL top; and iii)  
232 the vertical advection motion, carrying water vapour downward/upward through the interface  
233 between the ABL and FT. These three flux components are denoted as  $F_{local}$ ,  $F_{hadv}$ , and  $F_{vadv}$ ,  
234 and their contributions and evolutions will be discussed in the following.

### 235 3 Results and discussion

236 The present study is based on a 7-year flux calculation. The years 2011&2014-2019 are  
237 selected for analysis, which includes typical La Niña, El Niño, and neutral years (Marchukova  
238 et al., 2020; You et al., 2021; Felix Correia Filho et al., 2021), and are considered to be valid  
239 and concise datasets to reflect the characteristics of water vapour exchange between the ABL  
240 and FT. Their climatic representativeness is demonstrated using a long-term historical dataset  
241 provided by the fifth generation ECMWF (European Centre for Medium Range Weather  
242 Forecasts) reanalysis (Hersbach et al., 2023, download from the website  
243 <https://cds.climate.copernicus.eu/cdsapp#!/dataset/reanalysis-era5-pressure-levels?tab=form>).  
244 We compare the features of key meteorological elements during the study period (2011&2014-  
245 2019) and over the past 30 years (1990-2019) by the Kolmogorov-Smirnov test (K-S test) and  
246 histogram analysis. Temperature, three-dimensional wind component, specific humidity both  
247 near the surface and at the upper level, as well as the ABL height and precipitation, are  
248 concerned. The K-S test indicates that there is no significant difference (with a confidence level  
249 of 95%) between the 7-year sample period and the 30-year historical dataset for these variables  
250 (Table S3). The histogram analysis further illustrates that their normalized frequencies in the  
251 research samples are similar to those in the long-term historical data (Fig. S1). Also, the annual  
252 variation of the two sets of data presents a high consistency, with similar mean values and  
253 standard deviations (Fig. S2). The above analysis verifies that the 7-year samples adopted in  
254 this study can represent the long-term climatology, and be promising to obtain climatic features  
255 of water vapour exchange between the ABL and FT. The basic temporal and spatial patterns,

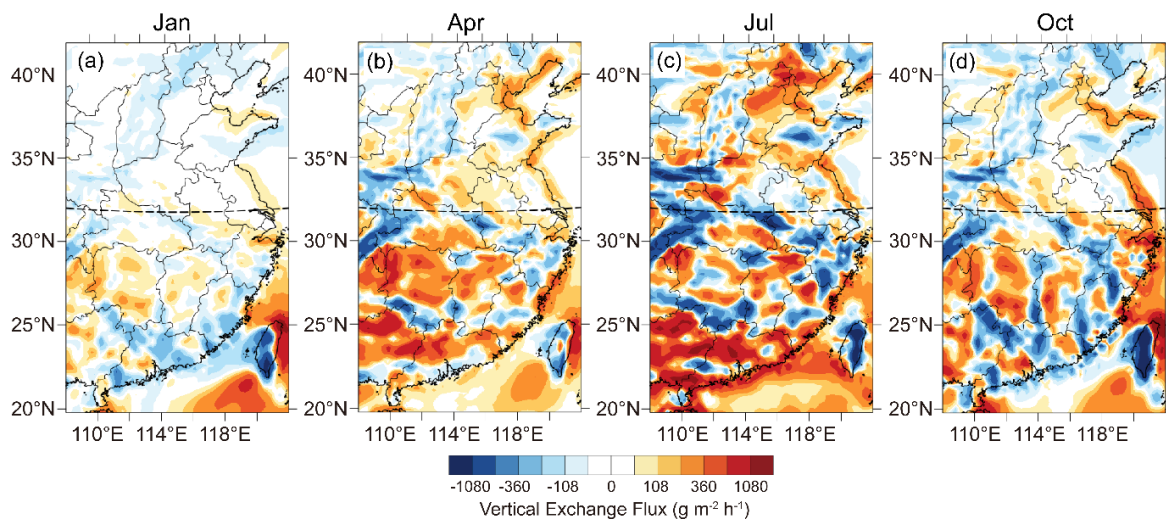


256 influencing mechanism, and relationship with ENSO and extreme precipitation are revealed as  
257 follows.

### 258 3.1 Seasonal generality and variability

#### 259 3.1.1 Spatial distribution

260 Figure 3 shows the spatial distribution of water vapour exchange flux between the ABL  
261 and FT in the research domain (20-42°N, 108-122°E, marked by red lines in Fig.1), averaged  
262 over all 7-year (2011, 2014-2019) for January, April, July, and October. It is obvious that the  
263 ABL-FT water vapour exchange in the south and north of the research domain is different,  
264 because they are affected by subtropical and temperate climates, respectively (Domroes and  
265 Peng, 1988; Zheng et al. 2013; Zhang et al., 2020). Therefore, the southern (20-32°N, 108-  
266 122°E) and northern (32-42°N, 108-122°E) regions are divided for analysis (the boundary is  
267 marked in Fig. 3). The water vapour exchange is more active in the southern region with more



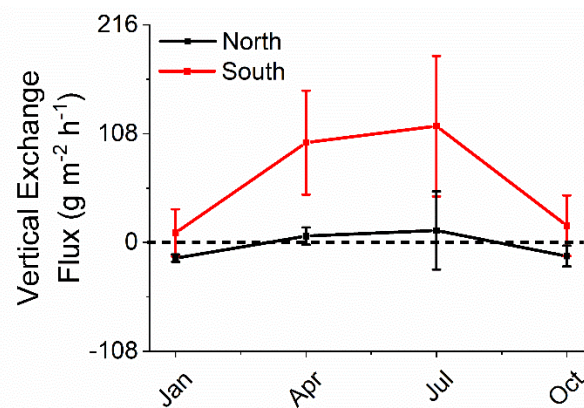
268  
269 Figure 3. Spatial distribution of ABL-FT water vapour exchange fluxes in eastern China, averaged over  
270 7 years for (a) January, (b) April, (c) July, and (d) October. Black dashed lines mark the boundary  
271 between the northern (32-42°N, 108-122°E) and southern (20-32°N, 108-122°E) regions. Positive and  
272 negative fluxes (warm and cool colours) represent water vapour upward and downward transport at the  
273 ABL and FT interface.

274 pronounced spatial variability, and tends to output from the ABL. In the northern region,  
275 vertical exchange fluxes and spatial differences are relatively small. From another perspective,  
276 the vertical exchange of water vapour is closely related to the topographic distribution (Fig.  
277 1b), which is manifested as strong exchange activities usually occurring around mountainous  
278 or coastal areas, both in the northern and southern regions. This feature is similar to the spatial  
279 pattern of the air mass exchange flux between the ABL and the FT indicated by Jin et al. (2021).  
280 It is the result of the dynamical interaction of topography on the synoptic system, and thermal  
281 property difference over the heterogeneous underlying surface (Kossmann et al., 1999; Dacre

282 et al., 2007; Jin et al., 2021). These phenomena will be detailedly explained in the mechanism  
283 analysis in Sect. 3.2.

### 284 3.1.2 Seasonal difference

285 Corresponding to Fig. 3, the spatial means of ABL-FT water vapour exchange flux and  
286 their seasonal evolutions for northern and southern regions are shown in Fig. 4. They are  
287 obtained by grid averaging in the ranges of 32-42°N, 108-122°E and 20-32°N, 108-122°E,  
288 respectively. Obviously, the exchange flux varies from season to season in both regions. For  
289 the northern region, winter and autumn (represented by January and October, respectively) are  
290 characterized by water vapour transport downward from the FT into the ABL, with the spatial  
291 mean fluxes of  $-15.6$  and  $-18.8 \text{ g m}^{-2} \text{ h}^{-1}$  ( $1 \text{ g m}^{-2} \text{ h}^{-1} = 10^{-3} \text{ mm h}^{-1}$ ) and the standard deviation  
292 of  $3.6$  and  $8.6 \text{ g m}^{-2} \text{ h}^{-1}$  over 7 years. While in spring and summer (represented by April and  
293 July, respectively), the northern region as a whole presents an upward export of water vapour  
294 from the ABL to the FT, with the regional mean fluxes being  $6.4$  and  $11.9 \text{ g m}^{-2} \text{ h}^{-1}$ . They are  
295 characterized by more significant inter-annual variations than the exchange fluxes in the cold  
296 seasons. In the southern region, the water vapour vertical exchange is featured with ABL output  
297 in all seasons, with a winter minimum and a summer maximum. The mean upward fluxes vary  
298 greatly, showing one order of magnitude greater in April and July ( $99.1$  and  $115.51 \text{ g m}^{-2} \text{ h}^{-1}$ )  
299 than in January and October ( $9.6$  and  $16.7 \text{ g m}^{-2} \text{ h}^{-1}$ ), accompanied by the larger standard  
300 deviation ( $50.4$  and  $68.4 \text{ g m}^{-2} \text{ h}^{-1}$ ). The notable interannual variability in the warm season may  
301 be related to the ENSO phenomenon, which will be discussed in the following section.



302  
303 Figure 4. Seasonal variation of average ABL-FT water vapour exchange fluxes and their standard  
304 deviations over the northern region (32-42°N, 108-122°E) and southern region (20-32°N, 108-122°E)  
305 during 7 years. Positive and negative fluxes represent water vapour upward and downward transport  
306 between the ABL and FT.

307 In order to better understand the magnitude of water vapour exchange between the ABL  
308 and FT, we compare the transport flux with the surface evaporation rate (Table 1). It indicates  
309 the “emission intensity” of water vapour from the surface, which varies in different regions and  
310 seasons. The surface evaporation rates in the northern and southern regions have maximums in  
311 summer ( $122.4 \text{ g m}^{-2} \text{ h}^{-1}$  and  $194.4 \text{ g m}^{-2} \text{ h}^{-1}$ ) and minimums in winter ( $21.6 \text{ g m}^{-2} \text{ h}^{-1}$  and  $108.0$

312  $\text{g m}^{-2} \text{h}^{-1}$ ). Obviously, the evaporation in the north is weaker than that in the south, especially  
 313 in winter, it is only one-fifth of that in summer. Consequently, for the northern region, during  
 314 the cold seasons with the dry land surface, the ABL-FT water vapour exchange is downward  
 315 and the input flux is 37%-72% of the surface evaporation rate. Although the specific humidity  
 316 decreases with height, counter-gradient transport still occurs reasonably because the ABL-FT  
 317 exchange is a typically non-local mixing process (Stull 1988; van Dop and Verver, 2001;  
 318 Ghannam et al., 2017). This suggests the ABL is a net moisture sink of upper layer FT air,  
 319 which plays a role in maintaining water vapour within this layer. As surface evaporation  
 320 intensifies in the warm months, water vapour is exported from the ABL in April and July, and  
 321 the upward flux accounts for 10% of the evaporation rate. In the southern region with relatively  
 322 strong evaporation, the ABL water vapour is always transported upward to the FT. The output  
 323 flux is about 10% of the evaporation rate in January and October, and this ratio is as high as  
 324 60%-80% in April and July, indicating that the ABL acts as an effective water vapour source  
 325 to the upper atmosphere.

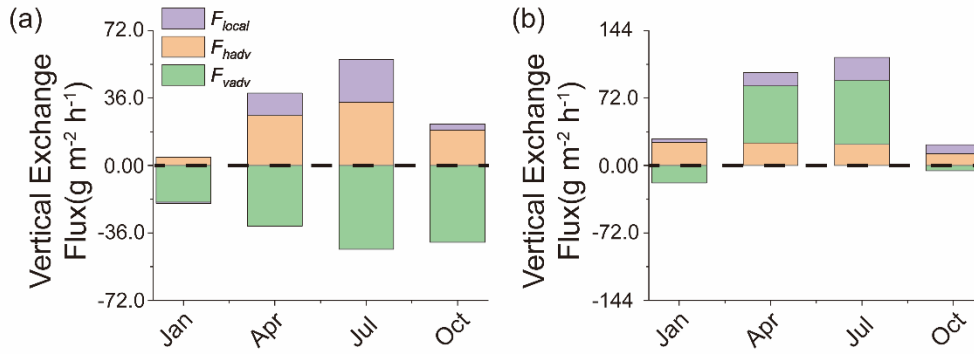
326 Table1. Comparison of ABL-FT water vapour exchange flux ( $\text{g m}^{-2} \text{h}^{-1}$ , positive for upward, negative  
 327 for downward) and surface evaporation rate ( $\text{g m}^{-2} \text{h}^{-1}$ , positive for upward) in the northern and southern  
 328 regions.

Region	Process	Jan	Apr	Jul	Oct
North	ABL-FT exchange	-15.6	6.4	11.9	-18.8
	Surface evaporation	21.6	61.2	122.4	50.4
South	ABL-FT exchange	9.6	99.1	115.5	16.7
	Surface evaporation	108.0	115.2	194.4	144.0

### 329 3.2 Main influential mechanism

330 As shown in Eq. (2), three physical terms contribute to the total ABL-FT exchange, i.e.,  
 331 the local temporal variation of ABL height ( $F_{local}$ ), the horizontal advection across the spatial  
 332 inclined ABL top ( $F_{hadv}$ ), and the vertical motion through the ABL-FT interface ( $F_{vadv}$ ). It is  
 333 of interest to clarify the specific effects of these factors on water vapour vertical exchange and  
 334 their seasonal characteristics. Results of the monthly mean and diurnal cycle over the 7 years  
 335 are presented below respectively.

336 The monthly mean results show that the term  $F_{vadv}$  is the most significant to total ABL-  
 337 FT moisture exchange flux (Fig. 5, green bar). In the northern region, this term produces  
 338 persistent downward flux ( $-19.5 \sim -44.7 \text{ g m}^{-2} \text{h}^{-1}$ , Fig. 5a), which substantially offsets the  
 339 upward flux caused by the other two terms, so that the ABL water vapour presents net input  
 340 during cold months (i.e., January and October) and weak output in warm seasons (i.e., April  
 341 and July). For the southern region, it induces small downward fluxes in January and October  
 342 ( $-18.6$  and  $-5.5 \text{ g m}^{-2} \text{h}^{-1}$ ) while large upward flux in April and July ( $60.7$  and  $68.6 \text{ g m}^{-2} \text{h}^{-1}$ ),  
 343 which results in the total water vapour exchange as weak and strong output from the ABL  
 344 during cold and warm months, respectively (Fig. 5b).

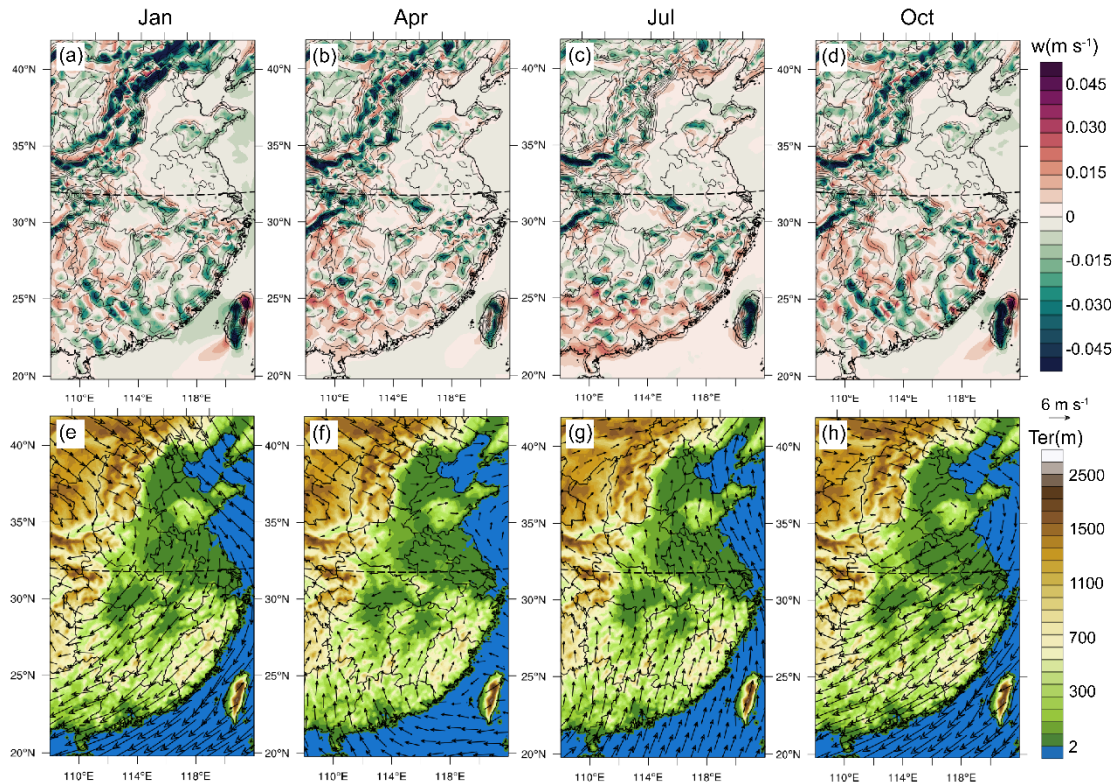


345

346 Figure 5. Contributions of three components ( $F_{local}$ ,  $F_{hadv}$ , and  $F_{vadv}$ ) to the total ABL-FT water  
 347 vapour exchange flux. Results are spatial mean over the (a) northern (32-42°N, 108-122°E) and (b)  
 348 southern (20-32°N, 108-122°E) regions of eastern China respectively.  $F_{local}$ : local temporal variation  
 349 of ABL height (purple bar);  $F_{hadv}$ : advection across the spatial inclined ABL top (yellow bar);  $F_{vadv}$ :  
 350 vertical motion through the ABL-FT interface (green bar). Positive and negative fluxes represent water  
 351 vapour upward and downward transport between the ABL and FT. The Y-axis scales are different in  
 352 (a) northern and (b) southern regions.

353 The upward/downward transport of water vapour caused by the term  $F_{vadv}$  depends on  
 354 the direction of the vertical motion. The spatial distributions of the vertical velocity are  
 355 presented in Fig. 6, accompanied by horizontal wind fields at the ABL top, as well as terrain  
 356 heights. The upward motions usually occur on the windward of the mountains, while the  
 357 descending velocities appear on the leeward side, in each season. This is attributed to the  
 358 dynamic forcing of the terrain on seasonal mean winds. Due to the alternation of winter and  
 359 summer monsoons throughout the year, the vertical motion pattern varies accordingly in four  
 360 representative months (Fig. 6a-d). In the winter, the Siberian high invades from the northwest  
 361 and forms strong northerly winds (Fig. 6e). In the northern region, the prevailing northwest  
 362 airflows overcome the obstruction of Taihang Mountain and intensely descend on its leeward  
 363 side (Fig. 6a). As the air migrates south, the dominant airflow deflects northeasterly (Fig. 6e),  
 364 and the vertical motion manifests more upward velocities in front of the major mountainous  
 365 region, and more downward velocities behind these mountains (Fig. 6a). During the summer,  
 366 southerly air flows dominate eastern China and gradually weaken from south to north (Fig. 6g).  
 367 The southern region is characterized by obvious forced uplift on the windward side of the major  
 368 mountains (Fig. 6c). The onshore airflow convergence of the prevailing southerly winds in  
 369 coastal areas also produces upward motions (Fig. 6c). These factors are conducive to the  
 370 vertical output of ABL water vapour in the southern region during warm months. The northern  
 371 region is less invaded by the summer monsoon: only the eastern part of the NCP is affected by  
 372 southerly winds to induce upward motion in the piedmont, while the western part is still  
 373 dominated by westerly winds leading to systematic subsidence (Fig. 6c, g). The general  
 374 patterns of vertical velocity fields provide an explanation for the water vapour exchange fluxes  
 375 caused by the term  $F_{vadv}$ . It is noticed that, although the ABL-FT water vapour exchange fluxes  
 376 in Fig. 3 are averages over 7 years, there still exists obvious spatial heterogeneity. Smooth  
 377 variations in both the mean wind field (Fig. 6e-h) and mean ABL height (Fig.S5) indicate these

378 two factors are not related to the flux heterogeneity. But there indeed exists discontinuous  
 379 structures in the vertical velocity fields at the ABL top (Fig.6a-d), which is significant to water  
 380 vapour exchange flux. There can be smaller-scale secondary vertical motion being stimulated  
 381 when prevailing airflows encounter diverse terrains (Fig. S4). Multiscale dynamical  
 382 interactions between complex terrain and synoptic processes should be of great significance to  
 383 the water vapour exchange between the ABL and FT.

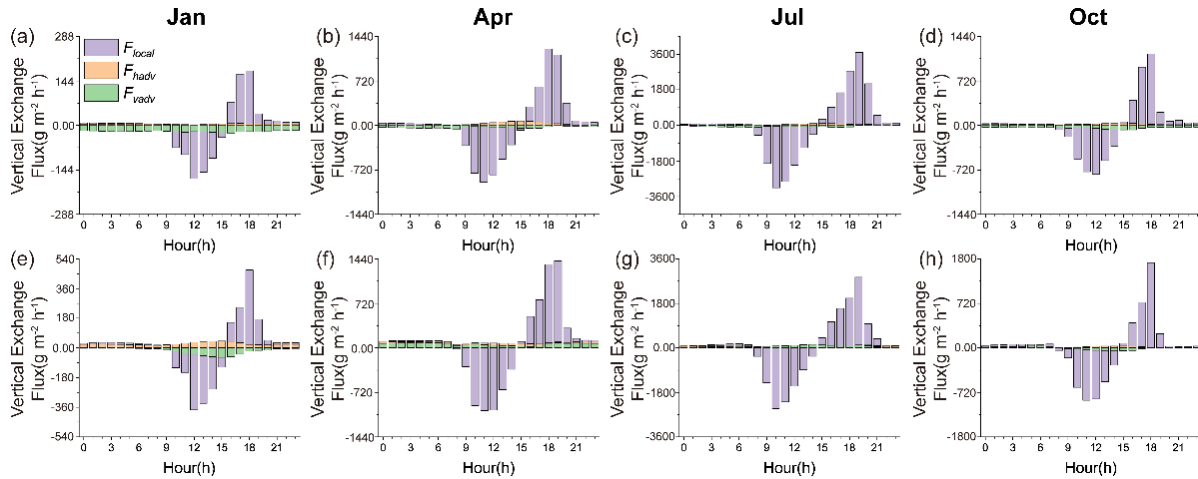


384  
 385 Figure 6. Spatial distribution of (a-d) vertical velocities at the ABL top and (e-h) terrain height  
 386 superposed with horizontal wind vectors averaged over 7 years for January, April, July, and October.  
 387 Positive values represent upward motions and the contours in (a-d) represent the terrain height. Black  
 388 dashed lines mark the boundary between the northern (32-42°N, 108-122°E) and southern (20-32°N,  
 389 108-122°E) regions.

390 The horizontal advection term  $F_{hadv}$  tends to allow water vapour to be out of the ABL  
 391 and the magnitude increases in spring and summer (Fig. 5, yellow bar). This water vapour  
 392 exchange component mainly occurs in the mountain-plain transition zone and the land-ocean  
 393 boundary (Fig. S3e-h), where the ABL is unevenly distributed due to the heterogeneous surface  
 394 properties (Fig. S5). During the warm season, the thermal difference is more obvious with the  
 395 solar radiation strengthening and thereby with larger spatial variation of the ABL, especially  
 396 in the northern region. This explains the seasonal variation of the water vapour exchange flux  
 397 caused by the term  $F_{hadv}$ .

398 The temporal ABL height variation term  $F_{local}$  contributes relatively less to the total water  
 399 vapour exchange (Fig. 5, purple bar). Noticeably, this average flux component is positive,  
 400 being negligible in autumn and winter ( $0.7\sim 3.3 \text{ g m}^{-2} \text{ h}^{-1}$ ), but becoming relatively pronounced

401 in spring and summer ( $12.0\sim 24.5\text{ g m}^{-2}\text{ h}^{-1}$ ). This is inconsistent with the air mass exchange  
 402 between the ABL and FT, in which the monthly average flux caused by this term is always  
 403 insignificant because the ABL entrainment and detrainment of the air mass cancel out each  
 404 other in a diurnal cycle (Jin et al., 2021). To understand more details of the term  $F_{local}$  in the  
 405 ABL-FT water vapour exchange, the mean diurnal variation of the exchange flux is derived  
 406 and shown in Fig. 7.



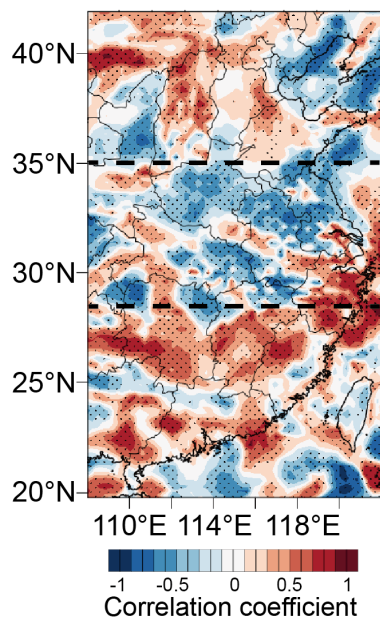
407

408 Figure 7. Diurnal variation of the three exchange flux components ( $F_{local}$ ,  $F_{hadv}$ , and  $F_{vadv}$ ) over the  
 409 (a-d) northern region ( $32\text{-}42^{\circ}\text{N}$ ,  $108\text{-}122^{\circ}\text{E}$ ) and (e-f) southern region ( $20\text{-}32^{\circ}\text{N}$ ,  $108\text{-}122^{\circ}\text{E}$ ) averaged  
 410 for (a, e) January, (b, f) April, (c, g) July, and (d, h) October.  $F_{local}$ : local temporal variation of ABL  
 411 height (purple bar);  $F_{hadv}$ : advection across the spatial inclined ABL top (yellow bar);  $F_{vadv}$ : vertical  
 412 motion through the ABL-FT interface (green bar). Positive and negative fluxes represent water vapour  
 413 upward and downward transport between the ABL and FT. The Y-axis scales are different in different  
 414 months and different regions.

415 At a first sight of the daily cycle,  $F_{local}$  is the absolutely dominant term in all seasons and  
 416 both northern and southern regions (Fig. 7, purple bar), corresponding to the diurnal variation  
 417 of the ABL height (shown in Fig. S6). When the unstable ABL develops in the morning, the  
 418 water vapour in the residual layer is entrained into the ABL; while as the daytime ABL  
 419 collapses in the later afternoon, a large part of water vapour is left aloft the newly formed stable  
 420 ABL. Note that, unlike the air mass exchange at the ABL top, the water vapour entrained  
 421 (input) flux is less than the output flux, especially in spring and summer. This difference can  
 422 be attributed to the fact that the surface is, in general, a continuous evaporation source  
 423 throughout a diurnal cycle. Turbulent mixing brings water vapour upward in the ABL depth,  
 424 and forms a net upward flux across the ABL top. This is also the reason why a larger magnitude  
 425 of  $F_{local}$  exists in the warm seasons when there is stronger surface evaporation. Although the  
 426 ABL temporal variation term  $F_{local}$  dominates the diurnal variation of the total ABL-FT  
 427 moisture exchange flux, it contributes only a weak net output of water vapour in a monthly  
 428 average flux, in comparison with the vertical motion term  $F_{vadv}$ , as mentioned above.

429 **3.3 Interannual variability and its relation with ENSO**

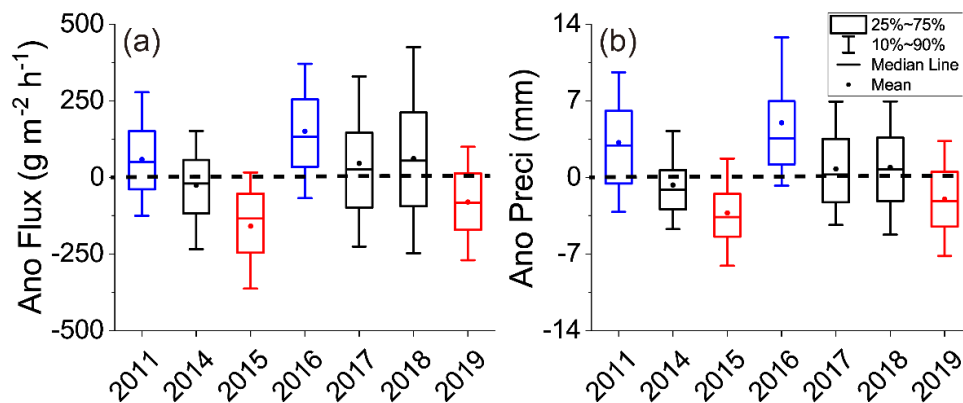
430 A climatic mean of the ABL-FT water vapour exchange over eastern China is presented  
431 above. Critically linked to the atmospheric water cycle, the exchange flux and its interannual  
432 variation are of great interest. It is well known that the atmospheric water cycle is significantly  
433 affected by El Niño and southern oscillation (ENSO), which is a joint phenomenon of the ocean  
434 and the atmosphere appearing as a recurring anomaly of the sea surface temperatures in the  
435 tropical Pacific and a seesaw of sea level pressure anomalies between Tahiti and Darwin. The  
436 El Niño (warm phase) and La Niña (cold phase) are the two extremes of ENSO (Walker and  
437 Bliss, 1932, 1937; Kousky et al., 1984; Wolter and Timlin, 2011). Considerable work has been  
438 conducted on the relationship between ENSO and wet and dry variability, water vapour  
439 horizontal transport, and precipitation events (Diaz, 2000; Knippertz and Wernli, 2010; Felix  
440 Correia Filho et al., 2021). However, little is known about the ABL-FT water vapour exchange  
441 during ENSO events. Here we take July as the research object, the month with the largest  
442 variability (shown in Fig. 4), to investigate the interannual difference of ABL-FT water vapour  
443 exchange fluxes affected by the ENSO phenomenon.



444  
445 Figure 8. Spatial distribution of correlation coefficient between the water vapour exchange flux  
446 anomalies and Niño-3.4 index in July for 7 years. The dots indicate statistically significant grids and  
447 the black dashed lines indicate the triple distribution.

448 The correlation between the water vapour exchange flux anomalies and the Niño-3.4 index  
449 during the study period (2011&2014-2019) is quantitatively calculated. The former (anomaly  
450 or variability) is derived from the difference of each year with the 7-year average, and the latter  
451 is obtained from the website [https://psl.noaa.gov/gcos\\_wgsp/Timeseries/Nino34/](https://psl.noaa.gov/gcos_wgsp/Timeseries/Nino34/), representing  
452 the average equatorial sea surface temperature across the Pacific from about the dateline to the  
453 South American coast (5°N-5°S, 170°W-120°W), which is the most commonly used indices to  
454 define El Niño and La Niña event. The statistical result shows that there is a significant

455 correlation between the two factors, with about 65% of the grids meeting the 95% confidence  
 456 level. A positive-negative-positive triple distribution is presented in the correlation map (Fig.  
 457 8). On this basis, the sensitive areas are identified, in which the water vapour exchange fluxes  
 458 are further analysed. The central region (28-35°N, 108-122°E) has the most obvious  
 459 significance, where the proportion of significant grids is as high as 70%. This area shows a  
 460 negative correlation, i.e., the mean vertical output flux of water vapour is enhanced by about  
 461 57.6~151.2  $\text{g m}^{-2} \text{h}^{-1}$  in cold phase La Niña years (2011 and 2016, blue boxes in Fig. 9a), and  
 462 vice versa in warm phase El Niño years (2015 and 2019, red boxes in Fig. 9a), and the flux  
 463 anomalies are close to 0 in neutral years (2014, 2017, and 2018, black boxes in Fig. 9a). In  
 464 south (20-28°N, 108-122°E) and north (35-42°N, 108-122°E) areas with positive correlation  
 465 coefficients, the trend is reversed. That is, the ABL moisture ventilation flux weakens  
 466 79.2~140.4  $\text{g m}^{-2} \text{h}^{-1}$  in La Niña years and increases 108~194  $\text{g m}^{-2} \text{h}^{-1}$  in El Niño years (figure  
 467 not shown). This provides an explanation for the interannual variation of the water vapour  
 468 exchange flux mentioned in Sect. 3.1.2.

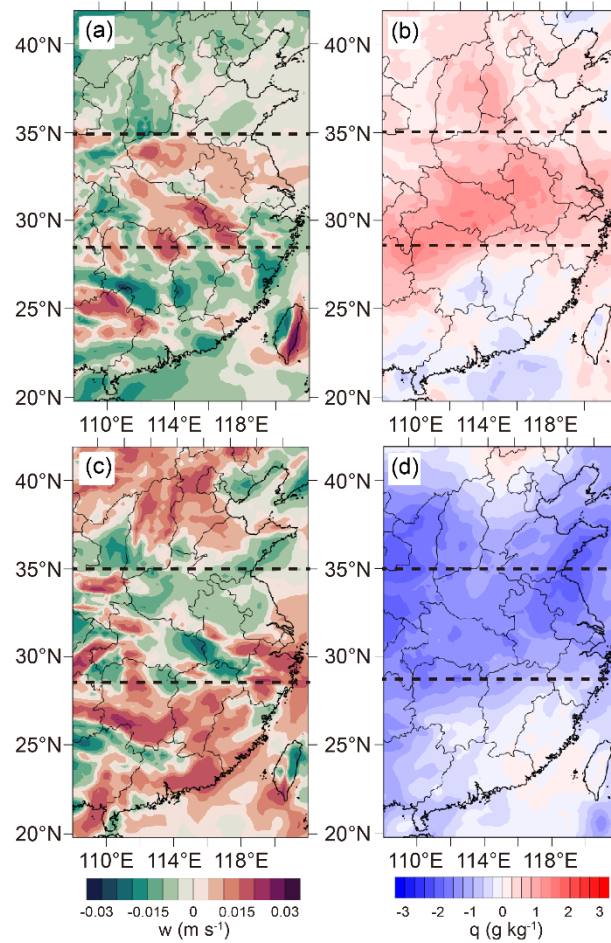


469  
 470 Figure 9. Anomalies of (a) water vapour exchange flux and (b) precipitation in July over the central  
 471 region (28-35°N, 108-122°E, indicated in Fig. 8) during 2011&2014-2019. Blue, red and black indicate  
 472 La Niña years, El Niño years and neutral years, respectively. Upper and lower sides of the box are the  
 473 75th and 25th percentile, and whiskers are the 90th and 10th percentile. Hollow squares and black lines  
 474 in the box are mean and median.

475 In order to elucidate why the water vapour vertical exchange flux varies with ENSO, we  
 476 further analyse three exchange components anomalies in El Niño and La Niña years (Fig. S7).  
 477 Among them, the term  $F_{vadv}$  presents the most obvious correspondence with the correlation  
 478 pattern (Fig.8), demonstrating that vertical motion and water vapour content at the ABL top  
 479 are crucial influencing factors. We select the central region (with the most significant  
 480 correlation) for detailed analysis. As shown in Fig.10, in La Niña year (represented by 2016),  
 481 the upward vertical velocity strengthened and the water vapour mixing ratio increased in the  
 482 central area, while the opposite trend was observed in El Niño year (represented by 2015). This  
 483 phenomenon is attributed to the stronger East Asian monsoon that brings more water vapour  
 484 from the south and facilitates convergence to uplift during the cold phase period of ENSO,  
 485 while in the warm phase, the weaker southerly wind reduces water vapour transport and is not



486 conducive to convergence within the ABL (Zhou et al. 2012; Xue et al., 2015; Gao et al., 2018),  
 487 which explains the increase or decrease of ABL water vapour output affected by ENSO.



488  
 489 Figure 10. Spatial distribution of anomalies of vertical velocities (left) and water vapour mixing ratio  
 490 (right) at the ABL top in July of (a-b) 2016 (La Niña year) and (c-d) 2015 (El Niño year).

491 Previous observation climatological studies have indicated that the summer precipitation  
 492 anomalies in La Niña/ El Niño years are characterized by a tripolar distribution over eastern  
 493 China (Wang et al., 2020), similar to water vapour exchange flux anomalies revealed in this  
 494 work. It is of interest to investigate the relationship between water vapour vertical exchange  
 495 and precipitation under the influence of ENSO. Taking the central region (28-35°N, 108-  
 496 122°E) as an example, the precipitation anomalies present a good correspondence with the  
 497 variations of the ABL-FT water vapour exchange flux (Fig. 9). Specifically, precipitation  
 498 increases (decreases) about 3.2-6.9 mm (2.8-3.5 mm) when the vertical output of water vapour  
 499 intensifies (weakens) in La Niña (El Niño) years. That is, enhanced water vapour output flux  
 500 from the ABL to the FT tends to produce increased precipitation and vice versa. These results  
 501 imply that, upper layer FT water vapour supplement from the ABL can also be a significant  
 502 factor in changing regional precipitation, in addition to horizontal transport.

503 It should be stated that the above results are preliminary and rough, due to the limitations  
 504 of the sample. The response of the ABL-FT water vapour exchange to ENSO, and its impact  
 505 on precipitation, are complicated. The isolated patches in Fig. 8 and Fig. 10, as well as the box

506 and whisker in Fig. 9 (being 75th-25th and 90th-10th percentile of the flux/precipitation  
507 anomalies), reflect the complex spatial variability over the research domain, which is not  
508 thoroughly analysed in the current work. Nevertheless, this general result points to an  
509 association among ABL-FT water vapour exchange, ENSO, and extreme precipitation, which  
510 should be paid more attention to in future research.

### 511 **3.4 Discussion**

512 The present results are based on numerical simulations. Although reasonable  
513 parameterization schemes are chosen according to sensitivity experiments, and the model  
514 performance is also evaluated by observational data, there are inevitable uncertainties in the  
515 modelled meteorological fields, which may directly affect the estimate of ABL-FT water  
516 vapour exchange flux. For example, the difference between the simulated ABL height and the  
517 observed value (~70 m and 120 m in winter and summer) brings ~30% uncertainty to the  
518 acquisition of vertical velocity at this level, which may affect the accuracy of the flux results  
519 in a similar magnitude. In addition, ignoring the turbulence term in this study may also reduce  
520 the accuracy of the results. Nevertheless, this work presents a general view of long-term and  
521 large-scale ABL-FT water vapour exchange over eastern China.

522 The water vapour exchange in the climatological sense presents a significant regional  
523 division of north and south China, due to their quite distinct climatic features. In addition to  
524 this general pattern, the spatial heterogeneity associated with the topographic distribution is  
525 also noteworthy. We try to sort out the vertical exchange fluxes of water vapour over the ocean,  
526 plain and mountain, roughly by the altitude below 0m, between 0-200m and greater than 200m.  
527 The statistical results show that the ocean and plain are characterized by the upward output of  
528 water vapour from the ABL, while the mountainous regions are dominated by downward  
529 transport. This mode reflects the important role of the complex terrain in causing ABL-FT  
530 vertical exchange. As described in Sect. 3.2, the prevailing airflow is obstructed by the  
531 mountains to forcingly ascend on the windward and densely descend on the leeward slope, then  
532 it decelerates and converges to induce upward motion when reaching the plain area. This  
533 vertical motion pattern makes the water vapour upward export from the ABL in the plain, and  
534 downward transport in mountainous areas due to the intensity and effect of the leeward side  
535 subsidence being larger than that of the uplift in the windward side. For the ocean area,  
536 horizontal wind crossing the inclined boundary layer top is responsible for the ABL water  
537 vapour output, especially in the nearshore region. We admit the current analysis is preliminary,  
538 but it does indicate the characteristics of vertical exchange flux distribution with topography,  
539 and the significance of the interaction between mountain/sea and synoptic airflow. This finding  
540 suggests that topographic ventilation is not only caused by mesoscale circulations such as  
541 daytime upslope winds/sea breezes around mountains/coasts (Henne et al., 2004; Weigel et al.,  
542 2007) or convective activities on a relatively small scale or a specific time (Gonzalez et al.,  
543 2016; Dahinden et al., 2021). Dynamical forcing of terrain on seasonal airflow or synoptic  
544 winds is more essential, which induces vertical motion and leads to systematic water vapour

545 exchange. The topographic-dependent feature of water vapour vertical exchange should also  
546 be of general meaning to other complex terrain regions around the world.

547 Moreover, the climatology of water vapour exchange flux between ABL and FT provides  
548 a quantitative background for investigating weather processes, radiation feedback and climate  
549 changes. Water vapour entering the FT may provide more latent heat to the energy flows and  
550 further affect synoptic systems. It is also involved in the radiative budget to influence climate.  
551 Previous model simulations and observations indicate that small yet systematic changes in the  
552 humidity of the upper atmosphere modulate the magnitude of the hydrological cycle and  
553 radiative feedback, including clouds and precipitation (Minschwaner and Dessler, 2004;  
554 Sherwood et al., 2010; Allan, 2012). Our results also demonstrate a notable relation between  
555 precipitation anomalies and ABL-FT water vapour exchange patterns. Based on the  
556 quantitative results in this study, the specific role of ABL - FT water vapour exchange in  
557 Earth's energy flows and climate system might be studied further in the future.

#### 558 **4 Conclusions**

559 In this study, we developed a climatology of water vapour exchange flux between the  
560 ABL and FT, based on 7-year meteorological modelling data. The ABL water vapour  
561 conservation method was used to estimate the vertical exchange flux across the ABL-FT  
562 interface. Spatial distribution and seasonal characteristics of the water vapour exchange were  
563 presented, and the influential mechanisms were analysed. The interannual difference was  
564 simply discussed through its variations with ENSO events. The major findings of this work are  
565 as follows:

566 (1) The spatiotemporal distribution of the ABL-FT water vapour exchange was  
567 characterized by regional division and seasonal variation. During January and October in the  
568 northern part (32-42°N), water vapour transport was downward to maintain ABL moisture,  
569 while in the southern region (20-32°N) it was persistently exported to moisture the FT, with  
570 the output flux from 10% to 80% of the surface evaporation rate.

571 (2) Vertical motion at the ABL-FT interface played a key role in the long-term (monthly  
572 or seasonal) average state of water vapour vertical exchange, which was caused by the dynamic  
573 forcing of the complex terrain on large-scale airflow. The temporal evolution of the vertical  
574 exchange flux over the course of one day was primarily driven by the diurnal cycle of the ABL  
575 height.

576 (3) Interannual variability of ABL-FT water vapour exchange was related to ENSO. Their  
577 correlation was shown as a triple anti-phase distribution, with exchange strengthening in the  
578 central zone and weakening in the north and south in La Niña years (and vice versa in El Niño  
579 years). It was mainly attributed to the alteration of vertical velocity and water vapour content  
580 at the ABL top varying with ENSO phases. Moreover, this pattern presented a good  
581 correspondence to the distribution of precipitation anomalies.

582 This work is the first trial to quantitatively reveal the climatological state of ABL-FT  
583 water vapour exchange flux over eastern China. Though for this specific research domain, the  
584 method and results derived in the present study may provide reference to other regions of the  
585 world. Through this study, the moisture linkage between the earth's surface and the upper layer  
586 atmosphere is more clearly described. This may help us to obtain a better understanding of the  
587 atmospheric water cycle.

#### 588 **Data availability**

589 The data in this study are available from the corresponding author (xhcai@pku.edu.cn).

#### 590 **Author contribution**

591 XHC and XPJ designed the research. LK and HSZ collected the data. XPJ performed the  
592 simulations and wrote the paper. XHC reviewed and commented on the paper. QQH, YS, XSW  
593 and TZ participated in the discussion of the article.

#### 594 **Competing interests**

595 The authors declare that they have no conflict of interest.

#### 596 **Acknowledgements**

597 This work was supported by National Key Research and Development Program of China  
598 (2018YFC0213204).

#### 599 **References**

- 600 Adebisi, A. A., Zuidema, P., and Abel, S. J.: The Convolution of Dynamics and Moisture with  
601 the Presence of Shortwave Absorbing Aerosols over the Southeast Atlantic, *Journal of*  
602 *Climate*, 28, 1997-2024, doi:10.1175/jcli-d-14-00352.1, 2015.
- 603 Allan, R. P.: The Role of Water Vapour in Earth's Energy Flows, *Surveys in Geophysics*, 33,  
604 557-564, doi:10.1007/s10712-011-9157-8, 2012.
- 605 Andrey, J., Cuevas, E., Parrondo, M. C., Alonso-Perez, S., Redondas, A., and Gil-Ojeda, M.:  
606 Quantification of ozone reductions within the Saharan air layer through a 13-year  
607 climatologic analysis of ozone profiles, *Atmospheric Environment*, 84, 28-34,  
608 doi:10.1016/j.atmosenv.2013.11.030, 2014.
- 609 Bailey, A., Toohey, D., and Noone, D.: Characterizing moisture exchange between the  
610 Hawaiian convective boundary layer and free troposphere using stable isotopes in water,

611 Journal of Geophysical Research-Atmospheres, 118, 8208-8221, doi:10.1002/jgrd.50639,  
612 2013.

613 Boutle, I. A., Beare, R. J., Belcher, S. E., Brown, A. R., and Plant, R. S.: The Moist Boundary  
614 Layer under a Mid-latitude Weather System, *Boundary-Layer Meteorology*, 134, 367-386,  
615 doi:10.1007/s10546-009-9452-9, 2010.

616 Boutle, I. A., Belcher, S. E., and Plant, R. S.: Moisture transport in midlatitude cyclones,  
617 *Quarterly Journal of the Royal Meteorological Society*, 137, 360-373, doi:10.1002/qj.783,  
618 2011.

619 Chen, F., and Dudhia J.: Coupling an advanced land surface-hydrology model with the Penn  
620 State-NCAR MM5 modeling system. Part I: Model implementation and sensitivity.  
621 *Monthly Weather Review*, 129(4), 569-585, doi:10.1175/1520-  
622 0493(2001)129<0569:caalsh>2.0.co, 2001.

623 Dacre, H. F., Gray, S. L., and Belcher, S. E.: A case study of boundary layer ventilation by  
624 convection and coastal processes, *Journal of Geophysical Research-Atmospheres*, 112,  
625 doi:10.1029/2006jd007984, 2007.

626 Dahinden, F., Aemisegger, F., Wernli, H., Schneider, M., Diekmann, C. J., Ertl, B., Knippertz,  
627 P., Werner, M., and Pfahl, S.: Disentangling different moisture transport pathways over the  
628 eastern subtropical North Atlantic using multi-platform isotope observations and high-  
629 resolution numerical modelling, *Atmospheric Chemistry and Physics*, 21, 16319-16347,  
630 doi:10.5194/acp-21-16319-2021, 2021.

631 Diaz, H. F. and Markgraf, V.: *El Niño and the Southern Oscillation: Multiscale Variability and*  
632 *Global and Regional Impacts*, Cambridge University Press: Cambridge, UK, 496 pp., ISBN  
633 0-521-621380-0, 2000.

634 Domroes, M. and Peng, G.: *The Climate of China*, Springer, Berlin, 361 pp., ISBN  
635 3540187685, 1988.

636 Dudhia, J.: Numerical study of convection observed during the winter monsoon experiment  
637 using a mesoscale two-dimensional model. *Journal of Atmospheric Sciences*, 46, 3077-  
638 3107, doi:10.1175/1520-0469(1989)046<3077:nsocod>2.0.co;2, 1989.

639 Felix Correia Filho, W. L., de Oliveira-Junior, J. F., da Silva Junior, C. A., and Santiago, D. d.  
640 B.: Influence of the El Niño-Southern Oscillation and the synoptic systems on the rainfall  
641 variability over the Brazilian Cerrado via Climate Hazard Group InfraRed Precipitation  
642 with Station data, *International Journal of Climatology*, 42, 3308-3322,  
643 doi:10.1002/joc.7417, 2022.

644 Fritz, C. and Wang, Z.: A Numerical Study of the Impacts of Dry Air on Tropical Cyclone  
645 Formation: A Development Case and a Nondevelopment Case, *Journal of the Atmospheric*  
646 *Sciences*, 70, 91-111, doi:10.1175/jas-d-12-018.1, 2013.

647 Gao, Y., Wang, H. J., and Chen, D: Precipitation anomalies in the Pan-Asian monsoon region  
648 during El Niño decaying summer 2016, *International Journal of Climatology*, 38, 3618–  
649 3632, doi:10.1002/joc.5522, 2018.

650 Ghannam, K., Duman, T., Salesky, S. T., Chamecki, M., and Katul, G.: The non-local character  
651 of turbulence asymmetry in the convective atmospheric boundary layer, *Quarterly Journal*  
652 *of the Royal Meteorological Society*, 143, 494-507, doi:10.1002/qj.2937, 2017.

653 Gonzalez, A., Exposito, F. J., Perez, J. C., Diaz, J. P., and Taima, D.: Verification of  
654 precipitable water vapour in high-resolution WRF simulations over a mountainous  
655 archipelago, *Quarterly Journal of the Royal Meteorological Society*, 139, 2119-2133,  
656 doi:10.1002/qj.2092, 2013.

657 Gonzalez, Y., Schneider, M., Dyroff, C., Rodriguez, S., Christner, E., Elena Garcia, O.,  
658 Cuevas, E., Jose Bustos, J., Ramos, R., Guirado-Fuentes, C., Barthlott, S., Wiegele, A., and  
659 Sepulveda, E.: Detecting moisture transport pathways to the subtropical North Atlantic free  
660 troposphere using paired H<sub>2</sub>O-delta D in situ measurements, *Atmospheric Chemistry and*  
661 *Physics*, 16, 4251-4269, doi:10.5194/acp-16-4251-2016, 2016.

662 Grell, G. A., and Devenyi, D.: A generalized approach to parameterizing convection combining  
663 ensemble and data assimilation techniques, *Geophysical Research Letters*, 29,  
664 doi:10.1029/2002gl015311, 2002.

665 Gvozdkova, B. and Mueller, M.: Moisture fluxes conducive to central European extreme  
666 precipitation events, *Atmospheric Research*, 248, doi:10.1016/j.atmosres.2020.105182,  
667 2021.

668 Hagos, S. M. and Cook, K. H.: Dynamics of the West African monsoon jump, *Journal of*  
669 *Climate*, 20, 5264-5284, doi:10.1175/2007jcli1533.1, 2007.

670 Harries, J., Carli, B., Rizzi, R., Serio, C., Mlynczak, M., Palchetti, L., Maestri, T., Brindley,  
671 H., and Masiello, G.: The far-infrared Earth, *Reviews of Geophysics*, 46,  
672 doi:10.1029/2007rg000233, 2008.

673 Henne, S., Furger, M., and Prevot, A. S. H.: Climatology of mountain venting-induced elevated  
674 moisture layers in the lee of the Alps, *Journal of Applied Meteorology*, 44, 620-633,  
675 doi:10.1175/jam2217.1, 2005.

676 Hersbach, H., Bell, B., Berrisford, P., Biavati, G., Horányi, A., Muñoz Sabater, J., Nicolas, J.,  
677 Peubey, C., Radu, R., Rozum, I., Schepers, D., Simmons, A., Soci, C., Dee, D., and  
678 Thépaut, J. N.: ERA5 hourly data on pressure levels from 1940 to present. Copernicus  
679 Climate Change Service (C3S) Climate Data Store (CDS), doi: 10.24381/cds.bd0915c6,  
680 2023.

681 Hirota, N., Ogura, T., Tatebe, H., Shiogama, H., Kimoto, M., and Watanabe, M.: Roles of  
682 Shallow Convective Moistening in the Eastward Propagation of the MJO in MIROC6,  
683 *Journal of Climate*, 31, 3033-3047, doi:10.1175/jcli-d-17-0246.1, 2018.

684 Hong, S. Y., and Lim, J. J.: The WRF single-moment 6-class microphysics scheme (WSM6),  
685 *Journal of Korean Meteorological Society*, 42, 129-151, 2006.

686 Hong, S. Y., Noh, Y., and Dudhia, J.: A new vertical diffusion package with an explicit  
687 treatment of entrainment processes, *Monthly Weather Review*, 134, 2318-2341,  
688 doi:10.1175/mwr3199.1, 2006.

689 Hov, O., and Flato, F.: Convective redistribution of ozone and oxides of nitrogen in the  
690 troposphere over Europe in summer and fall. *Journal of Atmospheric Chemistry*, 28, 319-  
691 337, doi:10.1023/a:1005780730600, 1997.

692 Jain, S., and Kar, S. C.: Transport of water vapour over the Tibetan Plateau as inferred from  
693 the model simulations, *Journal of Atmospheric and Solar-Terrestrial Physics*, 161, 64-75,  
694 doi:10.1016/j.jastp.2017.06.016, 2017.

695 Jin, X. P., Cai, X. H., Huang, Q. Q., Wang, X. S., Song, Y., and Zhu, T.: Atmospheric Boundary  
696 Layer-Free Troposphere Air Exchange in the North China Plain and its Impact on PM2.5  
697 Pollution, *Journal of Geophysical Research-Atmospheres*, 126,  
698 doi:10.1029/2021jd034641, 2021.

699 Jin, X. P., Cai, X. H., Yu, M. Y., Song, Y., Wang, X. S., Kang, L., and Zhang, H. S.: Diagnostic  
700 analysis of wintertime PM2.5 pollution in the North China Plain: The impacts of regional  
701 transport and atmospheric boundary layer variation, *Atmospheric Environment*, 224,  
702 doi:10.1016/j.atmosenv.2020.117346, 2020.

703 Kain, J. S.: The Kain-Fritsch convective parameterization: An update, *Journal of Applied*  
704 *Meteorology*, 43, 170-181, doi:10.1175/1520-0450(2004)043<0170:tkcpau>2.0.co;2,  
705 2004.

706 Kiehl, J. T., and Trenberth, K. E.: Earth's annual global mean energy budget, *Bulletin Of The*  
707 *American Meteorological Society*, 78, 197-208, doi:10.1175/1520-  
708 0477(1997)078<0197:eagmeb>2.0.co;2, 1997.

709 Knippertz, P. and Wernli, H.: A Lagrangian Climatology of Tropical Moisture Exports to the  
710 Northern Hemispheric Extratropics, *Journal of Climate*, 23, 987-1003,  
711 doi:10.1175/2009jcli3333.1, 2010.

712 Kossmann, M., Corsmeier, U., de Wekker, S. F. J., Fiedler, F., Vogtlin, R., Kalthoff, N.,  
713 Gusten, H. and Neininger, B.: Observations of handover processes between the atmospheric  
714 boundary layer and the free troposphere over mountainous terrain. *Contributions to*  
715 *Atmospheric Physics*, 72, 329-350, 1999.

716 Kousky, V. E., Kagano, M. T., and Cavalcanti, I. F. A.: A review of the southern oscillation-  
717 oceanic-atmospheric circulation changes and related rainfall anomalies, *Tellus Series A*,  
718 36, 490-504, doi:10.1111/j.1600-0870.1984.tb00264.x, 1984.

719 Li, Q. H., Wu, B. G., Liu, J. L., Zhang, H. S., Cai, X. H., and Song, Y.: Characteristics of the  
720 atmospheric boundary layer and its relation with PM2.5 during haze episodes in winter in  
721 the North China Plain, *Atmospheric Environment*, 223,  
722 doi:10.1016/j.atmosenv.2020.117265, 2020.

723 Lin, Y. L., Farley, R. D., and Orville, H. D.: Bulk parameterization of the snow field in a cloud  
724 model. *Journal of Climate Applied Meteorology*, 22, 1065-1092, doi:10.1175/1520-  
725 0450(1983)022<1065:bpotsf>2.0.co;2, 1983.

726 Liu, B., Tan, X., Gan, T. Y., Chen, X., Lin, K., Lu, M., and Liu, Z.: Global atmospheric  
727 moisture transport associated with precipitation extremes: Mechanisms and climate change  
728 impacts, *Wiley Interdisciplinary Reviews-Water*, 7, 10.1002/wat2.1412, 2020.

729 Liu, S. Y., and Liang, X. Z.: Observed Diurnal Cycle Climatology of Planetary Boundary Layer  
730 Height, *Journal of Climate*, 23, 5790-5809, doi:10.1175/2010jcli3552.1, 2010.

731 Marchukova, O. V., Voskresenskaya, E. N., and Lubkov, A. S.: Diagnostics of the La Niña  
732 events in 1900–2018, *Earth Environmental Sciences*, 606, 012036, doi:10.1088/1755-  
733 1315/606/1/012036, 2020.

734 McKendry, I. G., and Lundgren, J.: Tropospheric layering of ozone in regions of urbanized  
735 complex and/or coastal terrain: a review, *Progress in Physical Geography*, 24, 329-354,  
736 doi: 10.1177/030913330002400302, 2000.

737 Minschwaner, K., and Dessler, A. E.: Water vapor feedback in the tropical upper troposphere:  
738 model results and observations. *Journal of Climate*, 17, 1272-1282, doi:10.1175/1520-  
739 0442(2004)017<1272:WVFITT>2.0.CO;2, 2004.

740 Miura, H., Satoh, M., Tomita, H., Noda, A. T., Nasuno, T., and Iga, S.-i.: A short-duration  
741 global cloud-resolving simulation with a realistic land and sea distribution, *Geophysical*  
742 *Research Letters*, 34, doi:10.1029/2006gl027448, 2007.

743 Mlawer, E. J., Taubman, S. J., Brown, P. D., Iacono, M. J., and Clough, S. A.: Radiative transfer  
744 for inhomogeneous atmospheres: RRTM, a validated correlated-k model for the longwave,  
745 *Journal of Geophysical Research: Atmospheres*, 102, 16663-16682,  
746 doi:10.1029/97jd00237, 1997.

747 Newell, R. E., Zhu, Y., and Scott, C.: Tropospheric rivers-a pilot-study, *Geophysical Research*  
748 *Letters*, 19, 2401-2404, doi:10.1029/92gl02916, 1992.

749 Perez, J. C., Garcia-Lorenzo, B., Diaz, J. P., Gonzalez, A., Exposito, F., and Insausti, M.:  
750 Forecasting precipitable water vapor at the Roque de los Muchachos Observatory,  
751 *Conference on Ground-Based and Airborne Telescopes III*, San Diego, CA, 2010 Jun 27-  
752 Jul 02, WOS:000285506700149, doi:10.1117/12.859453, 2010.

753 Pilinis, C., Seinfeld, J. H., and Grosjean, D.: Water-content of atmospheric aerosols,  
754 *Atmospheric Environment*, 23, 1601-1606, doi:10.1016/0004-6981(89)90419-8, 1989.

755 Qian, X., Yao, Y. Q., Wang, H. S., Zou, L., Li, Y., and Yin, J.: Validation of the WRF Model  
756 for Estimating Precipitable Water Vapor at the Ali Observatory on the Tibetan Plateau,  
757 *Publications of the Astronomical Society of the Pacific*, 132, doi:10.1088/1538-  
758 3873/abc22d, 2020.

759 Sherwood, S. C., Roca, R., Weckwerth, T. M., and Andronova, N. G.: Tropospheric water  
760 vaporm convection, and climate, *Reviews of Geophysics*, 48, doi:10.1029/2009rg000301,  
761 2010.

762 Sherwood, S. C.: Maintenance of the free-tropospheric tropical water vapor distribution 1.  
763 Clear regime budget, *Journal of Climate*, 9, 2903-2918, doi:10.1175/1520-  
764 0442(1996)009<2903:motfft>2.0.co;2, 1996.

765 Sinclair, V. A., Belcher, S. E., and Gray, S. L.: Synoptic Controls on Boundary-Layer  
766 Characteristics, *Boundary-Layer Meteorology*, 134, 387-409, doi:10.1007/s10546-009-  
767 9455-6, 2010.



768 Sodemann, H. and Stohl, A.: Moisture Origin and Meridional Transport in Atmospheric Rivers  
769 and Their Association with Multiple Cyclones, *Monthly Weather Review*, 141, 2850-2868,  
770 doi:10.1175/mwr-d-12-00256.1, 2013.

771 Stull, R. B.: *An Introduction to Boundary Layer Meteorology*. Kluwer Acad., Dordrecht,  
772 Netherlands, 670 pp, doi:10.1007/978-94-009-3027-8, 1988.

773 Sun, L., Shen, B. Z., and Sui, B.: A Study on Water Vapor Transport and Budget of Heavy  
774 Rain in Northeast China, *Advances in Atmospheric Sciences*, 27, 1399-1414,  
775 doi:10.1007/s00376-010-9087-2, 2010.

776 Tabazadeh, A., Santee, M. L., Danilin, M. Y., Pumphrey, H. C., Newman, P. A., Hamill, P. J.,  
777 and Mergenthaler, J. L.: Quantifying denitrification and its effect on ozone recovery,  
778 *Science*, 288, 1407-1411, doi:10.1126/science.288.5470.1407, 2000.

779 van Dop, H., and Verver, G.: Countergradient transport revisited, *Journal of Atmospheric*  
780 *Sciences*, 58, 2240-2247, doi: 10.1175/1520-0469(2001)058<2240:CTR>2.0.CO;2, 2001.

781 Walker, G. T., and Bliss, E. W.: World weather V., *Memoirs of the Royal Meteorological*  
782 *Society*, 4, 53-84, 1932.

783 Walker, G. T., and Bliss, E. W.: World weather VI., *Memoirs of the Royal Meteorological*  
784 *Society*, 4, 119-139, 1937.

785 Wang, L. J., Cai, C., and Zhang, H. Y.: Circulation characteristics and critical systems of  
786 summer precipitation in eastern China under the background of two types of ENSO events,  
787 *Transactions of Atmospheric Sciences*, 43, 617-629,  
788 doi:10.13878/j.cnki.dqkxxb.20180817002, 2020.

789 Weigel, A. P., Chow, F. K., and Rotach, M. W.: The effect of mountainous topography on  
790 moisture exchange between the "surface" and the free atmosphere, *Boundary-Layer*  
791 *Meteorology*, 125, 227-244, doi:10.1007/s10546-006-9120-2, 2007.

792 Wolter, K. and Timlin, M. S.: El Nino/Southern Oscillation behaviour since 1871 as diagnosed  
793 in an extended multivariate ENSO index (MEI.ext), *International Journal of Climatology*,  
794 31, 1074-1087, doi:10.1002/joc.2336, 2011.

795 Wong, S., Naud, C. M., Kahn, B. H., Wu, L., and Fetzer, E. J.: Coupling of Precipitation and  
796 Cloud Structures in Oceanic Extratropical Cyclones to Large-Scale Moisture Flux  
797 Convergence, *Journal of Climate*, 31, 9565-9584, doi:10.1175/jcli-d-18-0115.1, 2018.

798 Wu, J. R., Bei, N. F., Hu, B., Liu, S. X., Zhou, M., Wang, Q. Y., Li, X., Liu, L., Feng, T., Liu,  
799 Z. R., Wang, Y. C., Cao, J. J., Tie, X. X., Wang, J., Molina, L. T., and Li, G. H.: Is water  
800 vapour a key player of the wintertime haze in North China Plain?, *Atmospheric Chemistry*  
801 *and Physics*, 19, 8721-8739, doi:10.5194/acp-19-8721-2019, 2019.

802 Wypych, A., Bochenek, B., and Rozycki, M.: Atmospheric Moisture Content over Europe and  
803 the Northern Atlantic, *Atmosphere*, 9, doi:10.3390/atmos9010018, 2018.

804 Xue, F., Zeng, Q. C., Huang, R. H., Li, C. Y., Lu, R. Y., Zhou, T. J.: Recent Advances in  
805 Monsoon Studies in China, *Advances in Atmospheric Sciences*, 32, 206-229,  
806 doi:10.1007/s00376-014-0015-8, 2015.

807 You, T., Wu, R. G., Liu, G., and Chai, Z. Y.: Contribution of precipitation events with different  
808 consecutive days to rainfall change over Asia during ENSO years, *Theoretical and Applied*  
809 *Climatology*, 144, 147-161, doi:10.1007/s00704-021-03538-8, 2021.

810 Zhang, H. G., Hu, Y. T., Cai, J. D., Li, X. J., Tian, B. H., Zhang, Q. D., and An, W.: Calculation  
811 of evapotranspiration in different climatic zones combining the long-term monitoring data  
812 with bootstrap method, *Environmental Research*, 191, doi:10.1016/j.envres.2020.110200,  
813 2020.

814 Zheng, J., Bian, J., Ge, Q., Hao, Z., Yin, Y., and Liao Y.: The climate regionalization in China  
815 for 1981-2010, *Chinese Science Bulletin*, 58, 3088-3099, doi:10.1360/972012-1491, 2013.

816 Zhou, T. J., and Yu, R. C.: Atmospheric water vapor transport associated with typical  
817 anomalous summer rainfall patterns in China, *Journal of Geophysical Research-*  
818 *Atmospheres*, 110, doi:10.1029/2004jd005413, 2005.

819 Zhou, W., Chen, W., and Wang, D. X.: The implications of El Niño-Southern Oscillation signal  
820 for South China monsoon climate, *Aquatic Ecosystem Health & Management*, 15, 14–19,  
821 doi:10.1080/14634988.2012.652050, 2012.

822 Zhu, Y., and Newell, R. E.: A proposed algorithm for moisture fluxes from atmospheric rivers,  
823 *Monthly Weather Review*, 126, 725-735, doi:10.1175/1520-  
824 0493(1998)126<0725:apafmf>2.0.co;2, 1998.